Enhanced vertical mixing in the glacial ocean inferred from sedimentary carbon isotopes

Wilmes, Sophie-Berenice; Green, Mattias; Schmittner, A.

Communications Earth and Environment

ARTICLE

Check for updates

Enhanced vertical mixing in the glacial ocean inferred from sedimentary carbon isotopes

Sophie-Berenice Wilmes [1,2 ✉], J. A. Mattias Green [1] & Andreas Schmittner [2]

Reconstructing the circulation, mixing and carbon content of the Last Glacial Maximum ocean remains challenging. Recent hypotheses suggest that a shoaled Atlantic meridional overturning circulation or increased stratification would have reduced vertical mixing, isolated the abyssal ocean and increased carbon storage, thus contributing to lower atmospheric CO_2 concentrations. Here, using an ensemble of ocean simulations, we evaluate impacts of changes in tidal energy dissipation due to lower sea levels on ocean mixing, circulation, and carbon isotope distributions. We find that increased tidal mixing strengthens deep ocean flow rates and decreases vertical gradients of radiocarbon and δ^{13}C in the deep Atlantic. Simulations with a shallower overturning circulation and more vigorous mixing fit sediment isotope data best. Our results, which are conservative, provide observational support that vertical mixing in the glacial Atlantic may have been enhanced due to more vigorous tidal dissipation, despite shoaling of the overturning circulation and increases in stratification.

[1] School of Ocean Sciences, Bangor University, Menai Bridge, UK. [2] College of Earth, Ocean and Atmospheric Sciences, Oregon State University, Corvallis, OR, USA. ✉email: s.wilmes@bangor.ac.uk

Circulation and mixing of the deep ocean have been suggested as important drivers of glacial–interglacial changes in ocean carbon storage and atmospheric CO_2. A number of studies hypothesize decreases in vertical mixing during the Last Glacial Maximum (26.5–19 kyr BP; LGM) due to an increase in stratification[1–4], or a shoaling of the Atlantic meridional overturning circulation (AMOC)[5–7], which would have isolated the deep ocean, increased carbon storage there and thus contributed to lowering atmospheric CO_2. Other studies, however, have suggested enhanced tidal energy dissipation in the deep ocean, which would have increased mixing[8–15], but the effects of changes in tidal mixing on ocean biochemical cycles and isotope distributions remain unknown and data constraints on deep LGM ocean mixing unexplored.

Tides provide an important energy source for internal mixing that sustains the ocean's meridional overturning circulation[16,17]. Surface (barotropic) tides lose energy through interactions with topographic features on the sea floor. A portion of that energy is dissipated locally, leading to turbulence and mixing there (near-field tidal mixing)[18,19]. The remainder of the energy is converted to internal waves (far-field internal tides) that propagate away from the generation sites and lead to mixing and dissipation elsewhere[19]. Since tidal mixing arises through interactions with topography, it is greatest near the sea floor and decreases towards the surface. It has been suggested[6] that a shallower interface between North Atlantic Deep Water (NADW) and Antarctic Bottom Water (AABW), as observed for the LGM, reduced mixing between the two water masses, thus isolating the deep ocean and increasing its carbon content. However, LGM sea level was approximately 120–130 m lower than at present and large additional ice sheets covered North America and northern Europe. The resulting changes in ocean depth and basin shape enhanced open-ocean tidal amplitudes, especially for the dominant semidiurnal tidal constituent M_2, and increased global tidal energy dissipation in the deep ocean during the LGM, with the most prominent enhancements in the North and South Atlantic. At present, the magnitude of the increase is not well constrained and highly sensitive to uncertainties in reconstructions of glacial ice sheet extent[13,14]. Stronger tidal mixing and increased diapycnal diffusion could have strengthened the meridional overturning circulation[14,20].

While there is agreement that the LGM AMOC was shallower than today[21–24], its strength remains a contentious subject with estimates ranging from a weaker[7,22,24,25] to a similar or stronger circulation[23,26,27]. Most studies assessing model versus paleo data to reconstruct the meridional overturning circulation have not considered tidal mixing changes[25,28,29], or if they did, simplified horizontally nonvarying diffusivities were used[23,30].

The aims of this study are to (1) evaluate the possible impact of LGM near-field tidal mixing changes on carbon isotope distributions in the glacial Atlantic, (2) to assess whether the existing carbon isotope measurements from LGM sediments provide constraints on vertical mixing, and (3) consider uncertainties in AMOC and tidal energy dissipation. Building on previous work[14,24] and using an intermediate-complexity global coupled physics and biogeochemistry model that includes near-field tidal mixing, we create an ensemble of LGM circulation states forced with different tidal dissipation estimates and modified atmospheric meridional moisture transport. The latter alters the buoyancy forcing in the Southern Ocean. Since changes in far-field tidal dissipation are not included in our model, the results are conservative. The simulations are compared against radiocarbon and $\delta^{13}C$ distributions from LGM sediments[7,24,31–34]. While these data constrain AMOC depth efficiently they do not provide good constraints on AMOC strength[35]. Our results show that simulations with a shallower and weaker AMOC and more vigorous tidal mixing fit the LGM carbon isotope data best. This suggests that vertical mixing in the glacial Atlantic Ocean may have been enhanced, and not reduced.

Results

Near-field tidal mixing effects on Atlantic circulation and water mass structure. Sampling AMOC and tide uncertainties, we have generated an ensemble of LGM model circulation states by modifying the Southern Hemisphere moisture diffusivity (μ_{SH})[24] and applying three different tidal dissipation cases from Wilmes et al.[14]: present day (PD) with 1 TW (1 TW = 10^{12} W) global internal tide dissipation, LGM ICE-6G (1.8 TW) and LGM ICE-5G (3.6 TW) (see "Methods" for details and Fig. 1 for run names). The two LGM tide cases result mainly from differences in land ice extent reconstructions, such as in the Weddell Sea, where the position of the grounding line remains uncertain. Figure 1 shows Atlantic streamfunctions for the ensemble. For PD tide forcing, AMOC strengths (here, maximum northward streamfunction at 25°N) range from a shutdown circulation state to an AMOC strength of 13.2 Sv (1 Sv = 10^6 m^{3}s^{-1}). For the simulations with LGM tide forcing, AMOC strengths range from 7.4 Sv to 15.1 Sv (ICE-6G tides) and 8.8 Sv to 16.7 Sv (ICE-5G tides). Including LGM tidal mixing increases AMOC strengths by around 1–3 Sv. For equivalent AMOC strengths, the AABW circulation cell is enhanced in simulations with stronger tidal forcing (by ~0.5 Sv for ICE-6G tides and ~1 Sv for ICE-5G tides; see Fig. 2a). This leads to a shoaling of the AMOC by between 200 and 300 m in the cases with stronger tidal forcing in comparison with an equivalent-strength AMOC model forced with PD tides (Fig. 2b). Nevertheless, AMOC strength and depth are highly correlated in our LGM experiments, which makes it difficult to distinguish between the two properties.

Vertical diffusivities (k_v; equation (1)) are strongly enhanced in simulations with LGM tidal forcing (Fig. 3a) with globally averaged k_v values increased by factors of 1.8–2.1 and 1.4–1.6 for ICE-5G and ICE-6G tides, respectively, with respect to runs with PD tidal forcing. However, in the Atlantic, the diffusivity enhancements are much more pronounced (Fig. 3b): k_v increases by factors of 3.3–3.9 (ICE-5G) and 2.0–2.5 (ICE-6G) (Supplementary Fig. S3).

Mid-depth (2000–4000 m) increases in stratification, expressed as the buoyancy frequency squared (N^2), exceeding 50% relative to the preindustrial control (PIC) are seen for the simulations with AMOC strengths below 11 Sv and corresponding AMOC depths of less than 3000 m in all ocean basins (Figs. 3c and d and Fig. 2). Stratification also affects modeled diffusivities (see equations (2) and (1), respectively). This can be appreciated by comparing simulations with different AMOC states but identical tidal energy dissipation (Fig. 3c and d). Simulations with a strong and deep AMOC (e.g., i5gT 17Sv) show reduced stratification (N^2) and higher k_v compared with weak and shallow AMOC cases (e.g., i5g 10Sv). However, the effects of stratification on k_v are generally smaller than the effects of tidal energy dissipation (Fig. 3e and f), such that all simulations with LGM tides have higher diffusivities in the deep Atlantic than any of the simulations with PD tides. In the simulations using LGM tidal mixing, the relative increases in the energy-dissipation rate (ϵ) are much greater (up to 100% and 400% for ICE-6G globally and for the Atlantic, respectively, and more than twice that for ICE-5G tides), thus outcompeting the changes in N^2 and increasing k_v at all depths (Fig. 3).

For most simulations with fixed tidal energy dissipation, diffusivities at the interface between NADW and AABW (AMOC depth) decrease as the interface shoals (Fig. 2c), consistent with the hypothesis of Ferrari et al.[6]. However, interface diffusivities
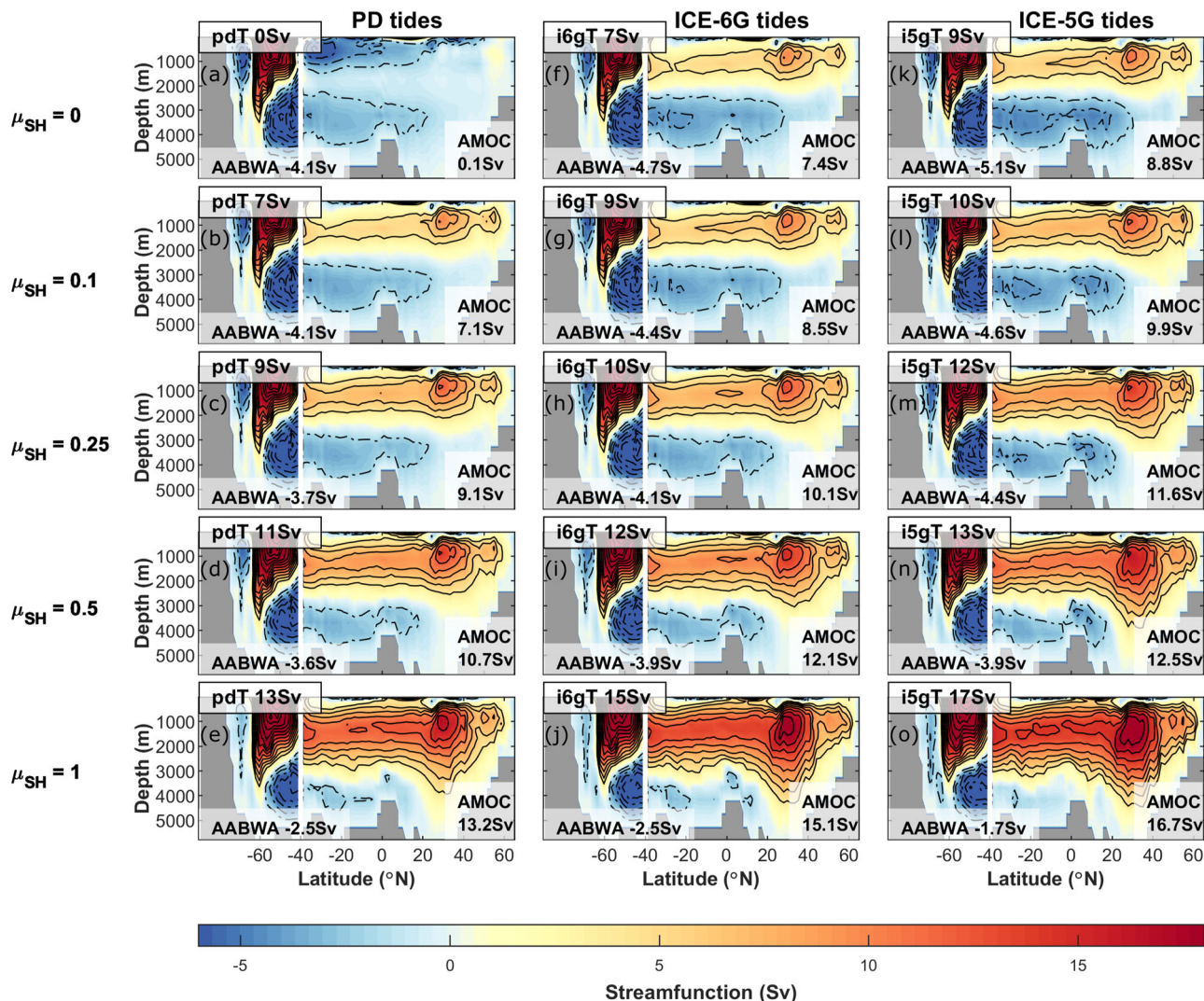
Fig. 1 Atlantic and Southern Ocean meridional overturning streamfunctions for the LGM simulation ensemble. Atlantic and Southern Ocean meridional overturning streamfunctions in Sv (1 Sv = 10^6 m^{3}s^{-1}) for the Last Glacial Maximum (LGM) simulation ensemble grouped by the tidal forcing and the μ_{SH} term. The Southern Ocean meridional streamfunction is plotted southward of 40°S, the Atlantic meridional streamfunction northward of 40°S. Their separation is indicated by the vertical white line at 40°S. Run names, given in the top left-hand corner for each panel, indicate the tidal dissipation case followed by the Atlantic meridional overturning streamfunction (AMOC) strength. AMOC strength at 25°N and Antarctic Bottom Water (AABW) strength in the Atlantic at 35°S are printed at the bottom of each panel. Simulations shown in panels (**a**)–(**e**) are forced with present-day (PD) global internal tide dissipation, simulations in panels (**f**)–(**j**) with LGM ICE-6G tidal dissipation, and runs shown in (**k**)–(**o**) with LGM ICE-5G tidal dissipation.

are larger for runs with LGM tides than for PD tides at similar AMOC strengths, which can compensate for the effects of AMOC shoaling. This means that, e.g., in the simulations with AMOC strengths of 9 Sv, k_v at the interface is enhanced by a factor of 2.5 for ICE-6G tides and 3.4 for ICE-5G tidal mixing.

Model—sediment isotope comparison. Atlantic radiocarbon distributions display strong circulation imprints (Supplementary Fig. S4). Generally, northward of ~30°S, southern-sourced waters occupying the lower part of the water column have older radiocarbon ages than waters sourced from the north. Southward of ~30°S, the entire water column is dominated by southern-sourced waters, and its structure, in contrast to the north, shows little change in response to the circulation changes (Supplementary Fig. S8). Weak and shallow AMOC cases have older radiocarbon ages in the deep ocean than those with stronger and deeper AMOC. Simulations with LGM tidal mixing show more gradual gradients separating southern-sourced from northern-sourced

water masses in the central and North Atlantic compared with PD tide models, for which gradients are sharper. Water masses occupying the deep North Atlantic have younger ages in the LGM tidal mixing cases than equivalent AMOC strength models with PD tidal mixing. A very similar picture emerges for the δ^{13}C distributions (Supplementary Figs. S5 and S7). Again, a strong circulation imprint is expressed, and cases with more mixing show reduced vertical gradients and less negative δ^{13}C values at depth for an equivalent AMOC strength. The largest discrepancies between modeled and sediment isotope compositions are seen in the deep South Atlantic where modeled values are isotopically too light and ages too young.

Calculations of root-mean-square (RMS) errors between modeled and reconstructed radiocarbon ages and δ^{13}C reveal a strong dependence on AMOC strength/depth, both globally and for the Atlantic (Fig. 4a–d). The lowest RMS errors are found for AMOC strengths of 8–10 Sv and AMOC depths of 2.4–2.7 km, and the highest errors for the cases with either a shutdown or a strong and deep AMOC. Simulations with stronger tidal mixing
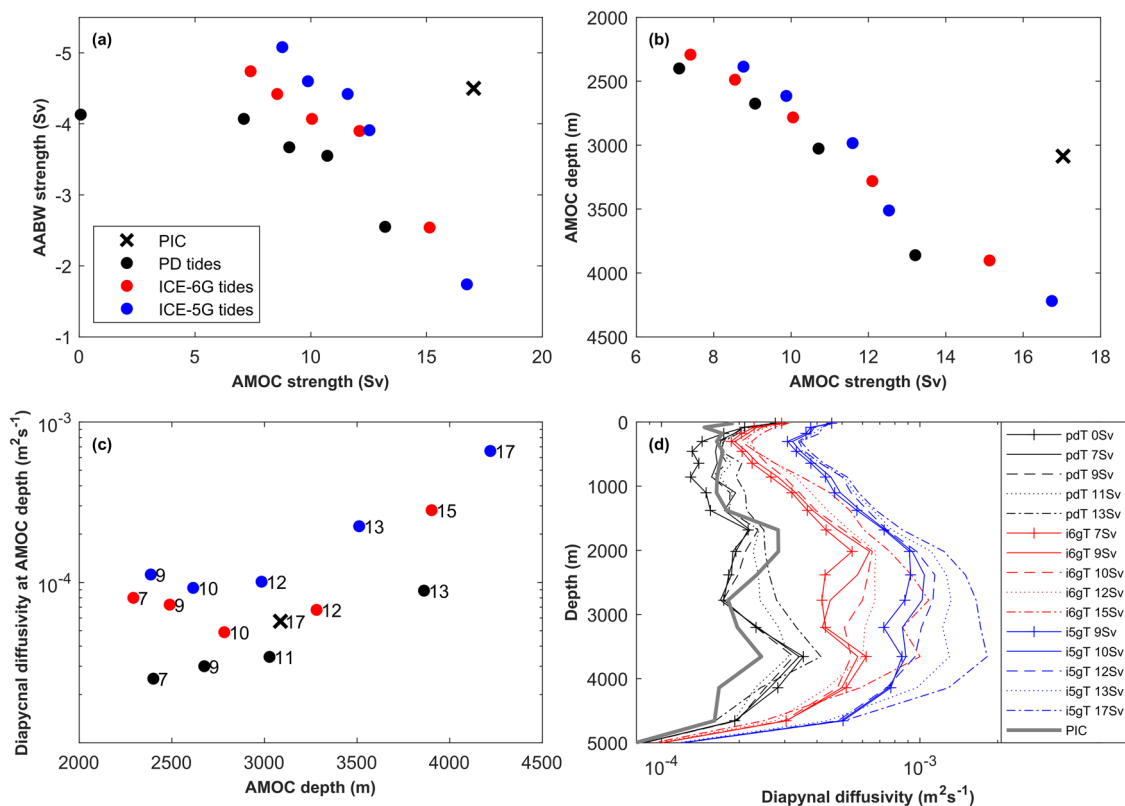
Fig. 2 Relationship between Atlantic circulation structure and diapycnal diffusivities. (**a**) Atlantic meridional overturning streamfunction (AMOC) strength at 25°N versus Antarctic Bottom Water (AABW) strength in the Atlantic at 35°S for the simulation ensemble with markers colored by the tidal forcing. (**b**) AMOC strength versus AMOC depth (AMOC depth was determined as the depth of the zero streamfunction isoline between 30°N and 30°S, which also represents the interface between AABW and North Atlantic Deep Water) with markers colored by tidal forcing. (**c**) Horizontally averaged Atlantic diapycnal diffusivities between 30°S and 30°N at the base of the AMOC cell as determined by the depth of the zero-streamfunction isoline. AMOC strength for each simulation is listed next to the markers. (**d**) Vertical profiles of horizontally averaged Atlantic diapycnal diffusivities (k_v).

consistently have lower $\delta^{13}C$ RMS errors in the best-fitting AMOC strength/depth range than the simulations with PD tides (Fig. 4b, c and d). Simulations i5gT 9Sv, i5gT 10Sv and i6gT 9Sv show the best fit in the Atlantic for both radiocarbon ages and $\delta^{13}C$. Simulation i5gT 9Sv decreases the global $\delta^{13}C$ RMS error by 8%, and in the Atlantic between 30°S and 50°N it improves the fit with the radiocarbon and $\delta^{13}C$ data by 15% and 9%, respectively, in comparison with the best-fitting run with PD tidal mixing and an AMOC strength of 9 Sv. We argue that Atlantic data provide more direct constraints on these simulations than global data since the largest changes in mixing occur in the Atlantic, and Pacific isotope distributions will be affected by additional uncertainties such as changes in deep/intermediate water formation in the North Pacific[36] that were not sampled in our ensemble. More data are needed to reliably represent the deep South Atlantic and Atlantic Southern Ocean where data coverage is sparse and reconstructions of $\delta^{13}C$ are hampered by higher errors for the present[37]. It is further possible that some climate processes in the South Atlantic and Atlantic Southern Ocean are not fully represented as the very old radiocarbon and negative $\delta^{13}C$ values in the LGM observations are not reached in this ensemble.

The depth profiles in Fig. 4e–f and Supplementary Figs. S6–S9 illustrate a transition zone between ~2000 and 3500 m northward of the equator in which the water mass characteristics change from northern sourced to southern sourced. The vertical gradient in this zone is quite smooth in the observations. It becomes evident that models with weak AMOC states have too strong mid-depth gradients (e.g., pdT 7Sv or i6G 7Sv), whereas

simulations with an AMOC strength >12 Sv show a gradient that is too weak, and the profiles have too young radiocarbon ages and too positive $\delta^{13}C$ values at depth. Only three simulations, those with AMOC strengths of 8.5–10 Sv and ICE-5G and ICE-6G tidal forcing, lie fully within a standard deviation of the mean radiocarbon and $\delta^{13}C$ depth profiles (see Supplementary Fig. S6). They feature AMOC depths of ~2400–2600 m and Atlantic vertical diffusivities that are enhanced by a factor of 2–3.1 in comparison with the simulation with equivalent AMOC depth but present-day tidal forcing. The simulation with ICE-5G tidal mixing and an AMOC strength of 9 Sv shows the best fit for both carbon isotopes, giving a consistently close fit to the mean depth profiles together with the lowest overall RMS errors, both in the Atlantic and globally.

The fit between the LGM simulations and the carbon isotopes is largely determined by AMOC strength/depth, as indicated by the near collapse of all data onto roughly one curve in Fig. 4a–d— despite the large differences in tidal mixing. However, mixing effects emerge for experiments with best-fitting AMOC strengths/ depths for which LGM tides improve the agreement with the carbon isotopes compared with PD tides. This indicates that tracer distributions are influenced by vertical mixing, even if that influence is more subtle than the dominating effect of AMOC structure and thus advection.

Discussion

Shoaling of the NADW–AABW interface moves it away from the high-mixing regions near the sea floor and thus decreases diffusive exchange between those water masses. This effect[6] is
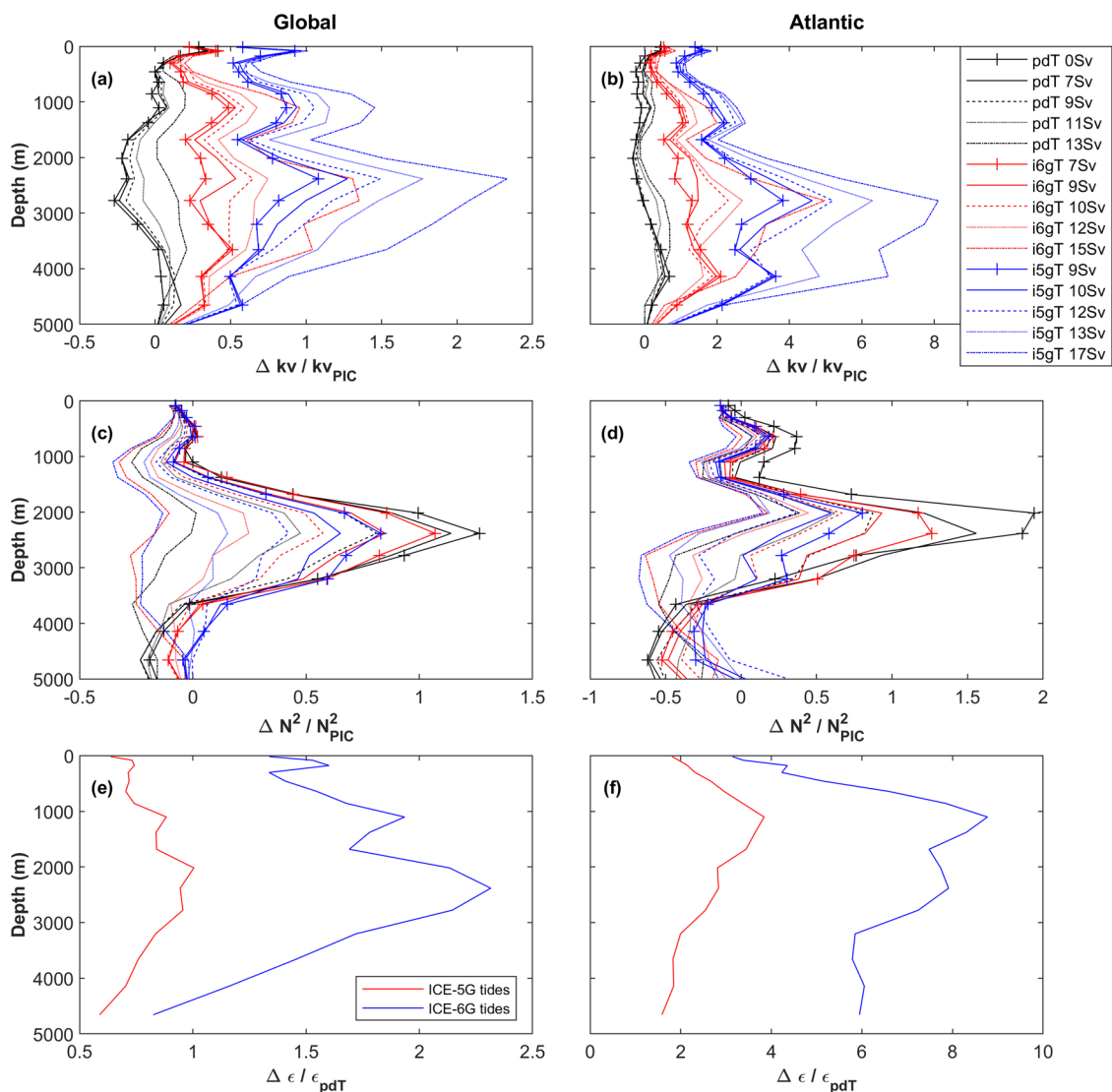
Fig. 3 Changes in vertical diffusivities, stratification, and turbulent energy dissipation. (right) Global and (left) Atlantic relative changes with respect to the preindustrial control (PIC) of (**a**) and (**b**) diapycnal diffusivities k_v, (**c**) and (**d**) stratification N^2 for the simulation ensemble. (**e**) and (**f**) relative changes in turbulent energy dissipation ϵ for ICE-6G and ICE-5G tides with respect to present-day (pd) tides.

captured in our experiments that show a general trend toward lower diffusivities with shallower AMOC depths for simulations with constant tidal dissipation (Fig. 2c). However, increased LGM tidal energy dissipation over-compensates for this effect, such that the three best-fitting LGM simulations (i5gT 9Sv, i5gT 10Sv, and i6gT 9Sv) have higher diffusivities on the NADW–AABW interface compared with the PIC simulation despite a shallower interface. In these runs, the remotely dissipated component is kept constant, however, it would be expected to increase in line with the locally dissipated tidal energy since most of the energy from the barotropic tide is transferred to internal waves that propagate away from the generation sites[19]. Considering these far-field effects would thus further increase LGM diffusivities. Our model assumes that far-field effects account for two-thirds of the total tidal energy dissipation. Although the partitioning into near- and far fields may be different[18], it would suggest that the effects of increased tidal mixing could be a factor of two larger than simulated here. On the other hand, the model under-estimates present-day AMOC depth and thus the degree of shoaling during the LGM. Assuming a modern AMOC depth at 25°N of 4.4 km from observations (Supplementary Fig. S1 [38]), the

PIC model predicts higher interface diffusivities in the modern tropical (30°S–30°N) Atlantic by about a factor of 2. Including higher latitudes leads to a smaller difference.

Our model-data comparison implies that vertical mixing rates in the glacial Atlantic, including the Atlantic sector of the Southern Ocean (Supplementary Fig. S10e), may have been enhanced. This contradicts conclusions from a number of studies that suggest reduced vertical mixing due to increased density stratification was an important factor in lowering atmospheric CO_2 during the LGM[1,6,2–4,39]. While our simulations do not infer direct mechanisms for the glacial atmospheric CO_2 drop, they include the effect of stratification changes on diffusivities and show that those effects could have been dwarfed by the impacts of increased tidal energy dissipation, which were not included by these studies. This therefore implies that reduced Atlantic vertical diffusivities may not have been the mechanism for increased Atlantic carbon storage, rather that carbon storage was enhanced, despite of more vigorous vertical mixing. Moreover, previous work[1] used potential density referenced to the surface to calculate changes in N_2, which overestimates the effects on k_v compared with using locally referenced potential density[40].
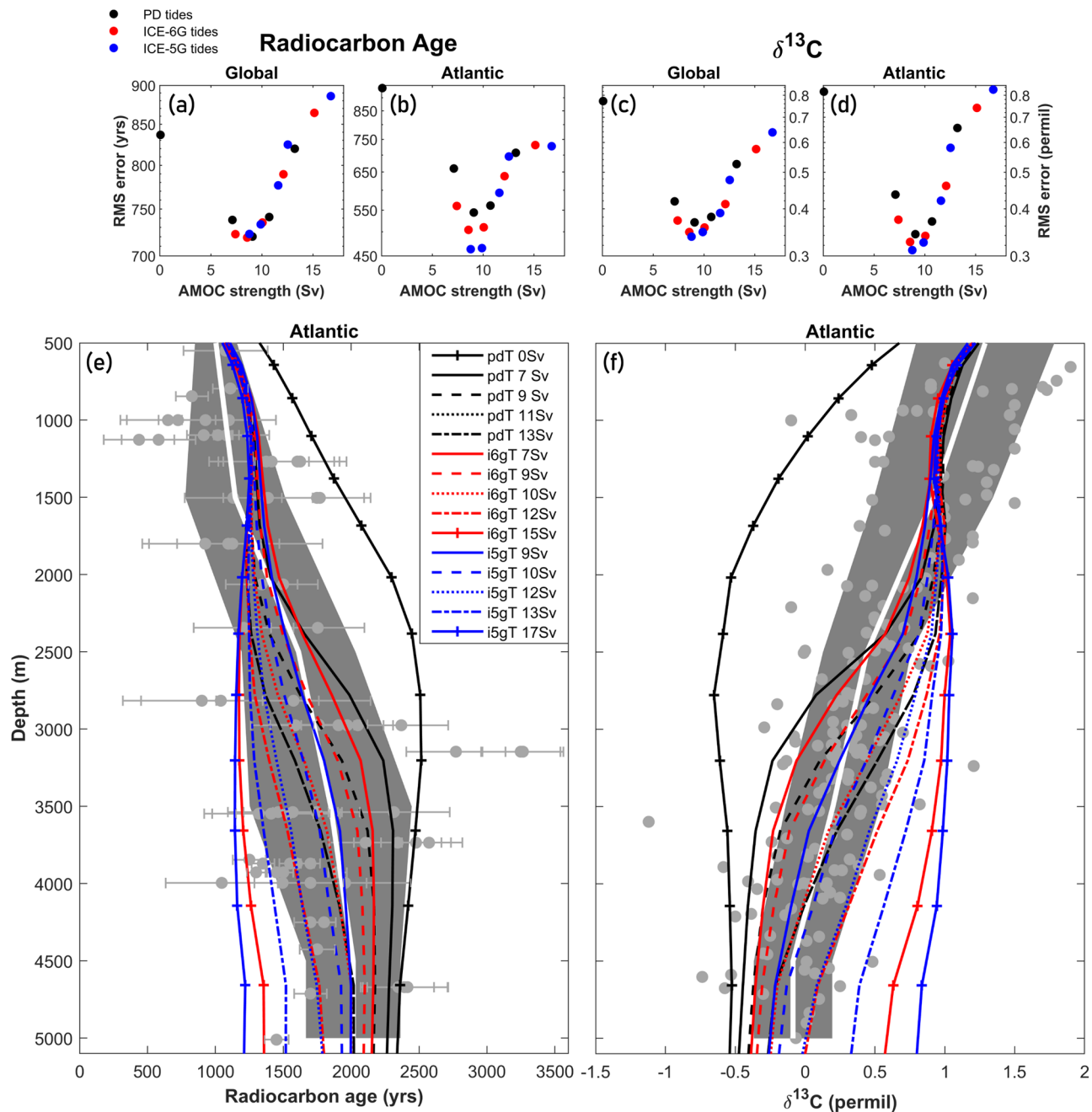
Fig. 4 Evaluation of modeled versus observational LGM radiocarbon and $\delta^{13}C$ distributions. (Top panel) Evaluation of modeled versus observational radiocarbon (**a** and **b**) and $\delta^{13}C$ (**c** and **d**) distributions plotted against Atlantic meridional overturning streamfunction (AMOC) strength for global (a and c) and Atlantic (30°S–50°N) (**b** and **d**) data. The data points are colored according to the tidal forcing applied in the respective simulation. Note the log-scale in panels (**a**)–(**d**) to distinguish the lowest root-mean-square (RMS) errors. (Bottom panel) Atlantic (30°S–50°N) depth profiles of Last Glacial Maximum radiocarbon (**e**) and $\delta^{13}C$ (**f**). The gray circle markers show observational data points. For the radiocarbon data points, the error bars represent a 1 σ uncertainty derived from the corresponding analytical uncertainties in radiocarbon dates and estimated uncertainties in reservoir ages[7]. The white line gives the mean value of the observations and the gray band indicates the $+/-1$ standard deviation around the mean. Model-depth profiles for a subset of simulations are shown in black, blue and red and are colored according to the tidal forcing. The legend gives the corresponding AMOC strength.

Based on analysis of oxygen isotope data, it has been suggested that the ratio between lateral transport and vertical mixing (Ψ/κ) during the LGM was increased by at least a factor of two compared with present day[5]. Here, we show that when we consider tidal mixing consistent with LGM ocean basin shape and depth, global diffusivities increase by a factor of 2–4 throughout the water column, with the strongest enhancements between 2000 and 4000 m. Compared with the modern ocean, the AMOC is reduced by about half in our best fitting simulations, which

suggests Ψ/κ was lower by a factor of 4–8, in contrast to Lund et al.'s[5] results. Our model does not include oxygen isotopes and thus we cannot assess the consistency of our simulations with those data.

More work is needed to quantify the effect of tidal mixing changes on carbon storage and atmospheric CO_2. Our best-fitting runs show similar carbon-storage values as the best fitting state in Muglia et al.[24] (within ~120 GtC; Supplementary Fig. S9), which was shown to explain more than three-quarters of the

glacial–interglacial CO_2 difference[41]. The same method could be used to analyze the experiments presented here, but based on the similarity in tracer distributions, we would expect similar effects on CO_2.

The AMOC strength may not be constrained well by the data[35] such that a shallow and strong AMOC state, which was not tested here, is possible[23]. However, compared with a shallow and weak AMOC state, a shallow and strong circulation would sharpen the mid-depth isotope gradients, which would require even more vertical mixing in order to fit the smooth gradient observed in the sediment data. It has been shown[42] that global ocean carbon content is more sensitive to AMOC depth than to AMOC strength. Thus, a strong and shallow AMOC with increased vertical mixing would presumably have a similar carbon content than the weak and shallow cases considered here.

It has been suggested[43,44], using a highly simplified ocean model setup with uniform globally uniform k_v, that in the present day, when diapycnal mixing rates are low, the mid-depth inter-hemispheric circulation is primarily set by the winds over the Southern Ocean and the associated upwelling they drive, and that the circulation structure is relatively insensitive to small changes in diapycnal mixing. However, it has been demonstrated[43,44] that a second circulation state may exist in the presence of much higher diapycnal mixing rates where the circulation and stratification structure are set by the diapycnal diffusivity and North Atlantic surface buoyancy distribution. The effect of the increased diapycnal mixing on the isopycnals (Fig. 9 in Nikurashin and Vallis[44]) can be seen when simulations pdT 9Sv and i5gT 9Sv are compared (Fig. S11), suggesting that altered LGM tides may be shifting the circulation from primarily wind driven to more diapynal mixing driven during the LGM.

The effects of increased tidal energy dissipation are likely underestimated in our model because we only consider the locally dissipated energy, while remotely dissipated energy is kept constant in the term k_{bg}. There are uncertainties in the proportions of near-field and far-field energy dissipation, and recent research points toward a spatially varying partitioning[18]. Furthermore, our current setup uses a fixed-exponential vertical decay scale, however, dynamic decay scales depending, e.g., on stratification have been proposed[45,46]. Future research should implement a parameterization of far-field effects[47], dynamic partitioning of locally and remotely dissipated energy, and allow the vertical decay scale to evolve between climates.

For the best-fitting circulation cases, increased LGM tidal mixing improves the fit to the Atlantic radiocarbon and $\delta^{13}C$ sediment data by around ~10–15%. This implies, contrary to the prevailing view in the literature[1–6,25] that LGM Atlantic vertical mixing may have been strengthened, rather than weakened, and it further highlights that explicit and relevant tidal energy sources need to be implemented in ocean circulation models. We show, for the first time to our knowledge, that sediment data provide constraints on past ocean mixing. The reconstruction method could be applied to other, relatively data-rich paleo periods.

Methods

Climate model. Here, the intermediate-complexity University of Victoria (UVic)[48,49] climate model, version 2.9, is used. The three-dimensional dynamical ocean model has a horizontal resolution of 3.6° × 1.8° and 19 vertical levels, and is coupled to a single-level 2D energy-moisture balance atmospheric component and a thermodynamic sea-ice model that allows sea ice to evolve in space and time. The climate model is run in the same setup as in Muglia et al.[24], apart from the tidal mixing, and thus includes LGM wind speed anomalies from simulations with fully coupled ocean-atmosphere general circulation models as part of the Paleoclimate Model Intercomparison Project (PMIP) version 3 ensemble.

UVic is coupled to the Model of Ocean Biogeochemistry and Isotopes (MOBI), version 1.8[24,50–52], which includes prognostic equations for phosphate, nitrate, dissolved and particulate iron, O_2, dissolved inorganic carbon, dissolved organic and particulate matter, zooplankton, and diazotrophs. MOBI includes an

advection–diffusion scheme, so tracers are influenced by both physical ocean dynamics and biogeochemical processes. For details on the prognostic ^{14}C cycle in the model, see Muglia et al.[24]. We use the same prescribed iron fluxes as Muglia et al.[24] for the preindustrial control simulation. For the LGM, we use their iron fluxes with enhancements by a factor of 10 in the Southern Ocean as these give the best fits to sediment nitrogen and carbon isotope data[24].

Near-field tidal mixing is implemented following Schmittner and Egbert[53] and as applied in Schmittner et al.[20] and Wilmes et al.[14]. It accounts for subgrid-scale bathymetric effects on the depth and spatial structure of the tidal energy input, and distinguishes between semidiurnal and diurnal tidal constituents. Three different tidal dissipation fields, taken from Wilmes et al.[14], were used for the LGM climate model simulations:

1. Present-day tidal dissipation (PD)
2. LGM ICE-5G tidal dissipation (LGM ICE-5G)
3. LGM ICE-6G tidal dissipation (LGM ICE-6G)

PD tidal dissipation was calculated from a tide model simulation using present-day ocean bathymetry. The LGM dissipation fields came from tide model runs using two different LGM ocean bathymetries based on the sea-level changes in the ICE-5G (VM L90) version 1.2[54] and ICE-6G (VM5a)[55,56] models. The tidal dissipation fields[14] have a horizontal resolution of 1/8° × 1/8° and include tidal energy losses for the principal diurnal and semi-diurnal tidal constituents M_2, S_2, K_1, and O_1. These fields were mapped onto the climate model grid using the methodology described in Schmittner and Egbert[53]. In the climate model, the diapycnal diffusivity k_v is given by

$$k_v = k_{bg} + \frac{\Gamma \epsilon}{N^2}, \qquad (1)$$

where k_{bg} is the background diffusivity with a value of $0.3 \times 10^{-4}\,\mathrm{m^2 s^{-1}}$, which includes remotely dissipated tidal energy (far-field) and mixing through other processes. Γ, the mixing efficiency, is set to 0.2, and N^2 is the buoyancy frequency. N^2 is expressed as

$$N^2 = -(g/\rho)(\partial \rho/\partial z), \qquad (2)$$

where g is the acceleration due to gravity, ρ is density, and z is depth in the water column. For details on the calculation of N^2 see Supplementary Methods S3. The rate of tidal energy dissipation, ϵ is given by

$$\epsilon = \frac{1}{\rho} \sum_{z'>z}^{H} \sum^{TC} q_{TC} D_{IT,TC}(x,y,z') F(z,z'), \qquad (3)$$

where $D_{IT,TC}(x,y,z')$ is the energy flux from the barotropic to the internal tide from the high-resolution tide model, D_{IT}, mapped onto the climate model grid accounting for subgrid-scale bathymetric effects in the vertical (thus the dependence on z'). F is the vertical decay function using an e-folding depth of 500 m above the sea floor H. q_{TC}, the local dissipation efficiency, accounts for the critical latitude y_c of diurnal and semidiurnal tidal constituents (TC):

$$q_{TC} = \begin{cases} 1, \text{for } |y| > y_{c,TC} \\ 0.33, \text{otherwise.} \end{cases} \qquad (4)$$

y_c is 30° for the diurnal constituents K_1 and O_1, and 72° for the semidiurnal constituents M_2 and S_2. It is important to note that the tidal mixing parameterization used here considers only changes in the locally dissipated energy, which amounts to only about one-third of the total energy dissipation. The remaining two-thirds is assumed to propagate away as internal waves and dissipate elsewhere. However, we do not account for changes in the remotely dissipated fraction, which is represented by a constant background diffusivity in our simulations. This is important for the interpretation of our results because it will make our simulations underestimate the true effects and thus be conservative.

Following Muglia et al.[24], we stepwise modify the Southern Hemisphere meridional moisture transport $F_{q,SH}$, which has been shown to alter Antarctic Bottom Water formation and AMOC strength[57], thus giving a spread of different AMOC states. In the calculation of specific moisture in UVic, the moisture eddy diffusivity term μ accounts for processes not resolved by advection. μ is the largest in the mid-latitudes where eddies play an important role. An offset term μ_{SH} is added in the Southern Hemisphere in order to increase the fit with observations. In our runs, we multiply μ_{SH} by factors of 0, 0.1, 0.25, 0.5, and 1 in order to achieve a suite of different ocean circulation states. Values lower than one decrease the meridional moisture flux and precipitation at high latitudes, which increases Southern Hemisphere sea-ice extent, increases salinity, surface pCO_2, and carbon content around Antarctica and thus of AABW, and enhances AABW flow rate and decreases the AMOC (see Supplementary Fig. S10a–d).

Aside from the preindustrial control (PIC), we run 15 LGM simulations (for setup details see Supplementary Methods S1), using each of the three tidal forcings (PD, LGM ICE-5G and LGM ICE-6G) in combination with the 5 μ_{SH} offset factors described above.

The PIC is evaluated in Supplementary Methods S2 and Tables S1 and S2. The PIC reproduces observed modern distributions of both isotopes well, such as lower (older) $\delta^{13}C$ (radiocarbon ages) in southern-sourced and higher (younger) values

in northern-sourced deep water (Supplementary Fig. S2). It is also consistent with observational estimates of circulation indices (Supplementary Table S1), although similar to other models, its modern AMOC depth at 25°N is too shallow (~3.1 km) compared with observational estimates (~4.4 km; see Supplementary Fig. S1 and Fig. 5 in Danabasoglu et al.[58]), which leads to too low (old) $\delta^{13}C$ (radiocarbon ages) in the abyssal North Atlantic (Supplementary Fig. S2).

Proxy data. We compare our modeled radiocarbon ages and $\delta^{13}C$ distributions to present-day and LGM radiocarbon and sediment isotope ratios. In total, 256 LGM radiocarbon age data points come from sediment data compiled by Skinner et al.[7] (see their work for details on the data). Outlier data points with ages greater than 6000 ^{14}Cyr were excluded, leaving a remainder of 246 points. Preindustrial water column radiocarbon ages were taken from the GLODAP[59] database for the locations of the LGM data. In total 434 preindustrial (core-top) and LGM $\delta^{13}C$ values from *Cibicides* foraminifera come from a global database[31]. Nine extra data points were added in the South Pacific[33,34] and one in the equatorial Atlantic[32]. In this work, we do not present results on $\delta^{15}N$ because several studies[24,51] demonstrate that $\delta^{15}N$ distributions are dominated by biological nutrient-utilization effects rather than circulation effects. An analysis (not shown) comparing LGM minus PIC $\delta^{15}N$ values for the simulations presented in this study with the $\delta^{15}N$ data from Muglia et al.[24] gives similar results to Muglia et al.[24] who show that simulations with the same Southern Ocean iron fluxes have similar errors, regardless of circulation structure.

Data availability
The model output is publicly available at https://zenodo.org/record/4704627#.YH7U5efTVPY[60]. Tidal dissipation files[61] are available at https://doi.org/10.5281/zenodo.1139242. The radiocarbon data used are available in the supplementary materials to Skinner et al.[7] (https://www.nature.com/articles/ncomms16010). The $\delta^{13}C$ data used[31–34] are available in the supplementary materials of Peterson et al.[31] (https://agupubs.onlinelibrary.wiley.com/doi/full/10.1002/2013PA002552), Burckel et al.[32] (https://cp.copernicus.org/articles/12/2061/2016/), Molina-Kescher et al.[33] (https://agupubs.onlinelibrary.wiley.com/doi/full/10.1002/2015PA002863), and Sikes et al.[34] (https://www.sciencedirect.com/science/article/pii/S0012821X1500802X?via%3Dihub).

Code availability
The UVic model code and run-setup files, together with the tidal dissipation and μ_{SH} files, are available in Supplementary Data S1.

References
1. Stein, K., Timmermann, A., Kwon, E. Y. & Friedrich, T. Timing and magnitude of southern ocean sea ice/carbon cycle feedbacks. *Proc. Natl Acad. Sci. USA* **117**, 4498–4504 (2020).
2. Watson, A. J. & Garabato, A. C. N. Southern Ocean mixing and upwelling in glacial-interglacial atmospheric CO_2 change. *Tellus* **58**, 73–87 (2006).
3. François, R. et al. Contribution of Southern Ocean surface-water stratification to low atmospheric CO_2 concentrations during the last glacial period. *Nature* **389**, 929–935 (1997).
4. Bouttes, N., Roche, D. M. & Paillard, D. Impact of strong deep ocean stratification on the glacial carbon cycle. *Paleoceanography* **24**, PA3203 (2009).
5. Lund, D. C., Adkins, J. F. & Ferrari, R. Abyssal Atlantic circulation during the Last Glacial Maximum: constraining the ratio between transport and vertical mixing. *Paleoceanography* **26**, PA1213 (2011).
6. Ferrari, R. et al. Antarctic sea ice control on ocean circulation in present and glacial climates. *Proc. Natl Acad. Sci. USA* **111**, 8753–8758 (2014).
7. Skinner, L. C. et al. Radiocarbon constraints on the glacial ocean circulation and its impact on atmospheric CO_2. *Nat. Commun.* **8**, 16010 (2017).
8. Egbert, G. D., Bills, B. G. & Ray, R. D. Numerical modeling of the global semidiurnal tide in the present day and in the last glacial maximum. *J. Geophys. Res.* **109**, C03003 (2004).
9. Arbic, B. K., MacAyeal, D. R., Mitrovica, J. X. & Milne, G. A. Ocean tides and Heinrich events. *Nature* **432**, 460 (2004).
10. Griffiths, S. D. & Peltier, W. R. Megatides in the Arctic Ocean under glacial conditions. *Geophys. Res. Lett.* **35**, L08605 (2008).
11. Griffiths, S. D. & Peltier, W. R. Modeling of polar ocean tides at the Last Glacial Maximum: amplification, sensitivity, and climatological implications. *J. Clim.* **22**, 2905–2924 (2009).
12. Green, J. A. M. Ocean tides and resonance. *Ocean Dyn.* **60**, 1243–1253 (2010).
13. Wilmes, S.-B. & Green, J. A. M. The evolution of tides and tidal dissipation over the past 21,000 years. *J. Geophys. Res. Oceans* **119**, 4083–4100 (2014).
14. Wilmes, S., Schmittner, A. & Green, J. A. M. Glacial ice sheet extent effects on modeled tidal mixing and the global overturning circulation. *Paleoceanogr. Paleoclimatol.* **34**, 1437–1454 (2019).
15. Velay–Vitow, J., Peltier, W. R. & Stuhne, G. R. The tides of the glacial ocean and their possible connection to Heinrich event instabilities of the laurentide ice sheet. *J. Geophys. Res. Oceans* **125**, e2019JC015444 (2020).
16. Wunsch, C. & Ferrari, R. Vertical mixing, energy, and the general circulation of the oceans. *Annu. Rev. Fluid Mech.* **36**, 281–314 (2004).
17. Ferrari, R. & Wunsch, C. Ocean circulation kinetic energy: reservoirs, sources, and sinks. *Annu. Rev. Fluid Mech.* **41**, 253–282 (2009).
18. Vic, C. et al. Deep-ocean mixing driven by small-scale internal tides. *Nat. Commun.* **10**, 1–9 (2019).
19. MacKinnon, J. A. et al. Climate process team on internal wave-driven ocean mixing. *Bull. Am. Meteorol. Soc.* **98**, 2429–2454 (2017).
20. Schmittner, A., Green, J. A. M. & Wilmes, S.-B. Glacial ocean overturning intensified by tidal mixing in a global circulation model. *Geophys. Res. Lett.* **42**, 4014–4022 (2015).
21. Gebbie, G. How much did Glacial North Atlantic water shoal? *Paleoceanography* **29**, 190–209 (2014).
22. Menviel, L. et al. Poorly ventilated deep ocean at the Last Glacial Maximum inferred from carbon isotopes: a data-model comparison study. *Paleoceanography* **32**, 2–17 (2017).
23. Kurahashi-Nakamura, T., Paul, A. & Losch, M. Dynamical reconstruction of the global ocean state during the Last Glacial Maximum. *Paleoceanography* **32**, 326–350 (2017).
24. Muglia, J., Skinner, L. C. & Schmittner, A. Weak overturning circulation and high Southern Ocean nutrient utilization maximized glacial ocean carbon. *Earth and Planet. Sci. Lett.* **496**, 47–56 (2018).
25. Howe, J. N. W. et al. North Atlantic deep water production during the Last Glacial Maximum. *Nat. Commun.* **7**, 11765 (2016).
26. Ritz, S. P., Stocker, T. F., Grimalt, J. O., Menviel, L. & Timmermann, A. Estimated strength of the Atlantic overturning circulation during the last deglaciation. *Nat. Geosci.* **6**, 208–212 (2013).
27. Lippold, J. et al. Deep water provenance and dynamics of the (de)glacial Atlantic meridional overturning circulation. *Earth Planet. Sci. Lett.* **445**, 68–78 (2016).
28. Amrhein, D. E., Wunsch, C., Marchal, O. & Forget, G. A global glacial ocean state estimate constrained by upper-ocean temperature proxies. *J. Clim.* **31**, 8059–8079 (2018).
29. Marzocchi, A. & Jansen, M. F. Connecting Antarctic sea ice to deep-ocean circulation in modern and glacial climate simulations. *Geophys. Res. Lett.* **44**, 6286–6295 (2017).
30. Ödalen, M., Nycander, J., Oliver, K. I., Brodeau, L. & Ridgwell, A. The influence of the ocean circulation state on ocean carbon storage and CO2 drawdown potential in an Earth system model. *Biogeosciences* **15**, 1367–1393 (2018).
31. Peterson, C. D., Lisiecki, L. E. & Stern, J. V. Deglacial whole-ocean $\delta^{13}C$ change estimated from 480 benthic foraminiferal records. *Paleoceanography* **29**, 549–563 (2014).
32. Burckel, P. et al. Changes in the geometry and strength of the Atlantic meridional overturning circulation during the last glacial (20-50 ka). *Clim. Past* **12**, 2061–2075 (2016).
33. Molina-Kescher, M. et al. Reduced admixture of North Atlantic deep water to the deep central South Pacific during the last two glacial periods. *Paleoceanography* **31**, 651–668 (2016).
34. Sikes, E. L., Cook, M. S. & Guilderson, T. P. Reduced deep ocean ventilation in the Southern Pacific Ocean during the last glaciation persisted into the deglaciation. *Earth Planet. Sci. Lett.* **438**, 130–138 (2016).
35. Gu, S. et al. Assessing the potential capability of reconstructing glacial Atlantic water masses and AMOC using multiple proxies in CESM. *Earth Planet. Sci. Lett.* **541**, 116294 (2020).
36. Rae, J. W. B. et al. Deep water formation in the North Pacific and deglacial CO2 rise. *Paleoceanography* **29**, 645–667 (2014).
37. Schmittner, A. et al. Calibration of the carbon isotope composition ($\delta^{13}C$) of benthic foraminifera. *Paleoceanogr. Paleoclimatol.* **32**, 512–530 (2017).
38. Moat, B. I. et al. Atlantic meridional overturning circulation observed by the RAPID-MOCHA-WBTS (RAPID-meridional overturning circulation and heatflux array-western boundary time series) array at 26N from 2004 to 2018 (v2018.2). (British Oceanographic Data Centre, National Oceanography Centre, NERC, UK, 2018).
39. Sigman, D. M., Hain, M. P. & Haug, G. H. The polar ocean and glacial cycles in atmospheric CO_2 concentration. *Nature* **466**, 47–55 (2010).
40. King, B. et al. Buoyancy frequency profiles and internal semidiurnal tide turning depths in the oceans. *J. Geophys. Res.* **117**, C04008 (2012).
41. Khatiwala, S., Schmittner, A. & Muglia, J. Air-sea disequilibrium enhances ocean carbon storage during glacial periods. *Sci. Adv.* **5**, eaaw4981 (2019).
42. Muglia, J. & Schmittner, A. Carbon isotope constraints on glacial Atlantic meridional overturning: strength vs depth. *Quat. Sci. Rev.* **257**, 106844 (2021).
43. Nikurashin, M. & Vallis, G. A theory of deep stratification and overturning circulation in the ocean. *J. Phys. Oceanogr.* **41**, 485–502 (2011).

44. Nikurashin, M. & Vallis, G. A theory of the interhemispheric meridional overturning circulation and associated stratification. *J. Phys. Oceanogr.* **42**, 1652–1667 (2012).

45. Polzin, k. L. An abyssal recipe. *Ocean Model.* **30**, 298–309 (2009).

46. Melet, A., Legg, S. & Hallberg, R. Climatic impacts of parameterized local and remote tidal mixing. *J. Clim.* **29**, 3473–3500 (2016).

47. Oblers, D. & Eden, C. A global model for the diapycnal diffusivity induced by internal gravity waves. *J. Phys. Oceanogr.* **43**, 1759–1779 (2013).

48. Weaver, A. J. et al. The UVic earth system climate model: Model description, climatology, and applications to past, present and future climates. *Atmos. Ocean* **39**, 361–428 (2001).

49. Eby, M. et al. Lifetime of anthropogenic climate change: millennial time scales of potential CO_2 and surface temperature perturbations. *J. Clim.* **22**, 2501–2511 (2009).

50. Somes, C. J. & Oschlies, A. On the influence of "non-Redfield" dissolved organic nutrient dynamics on the spatial distribution of N_2 fixation and the size of the marine fixed nitrogen inventory. *Glob. Biogeochem. Cycles* **29**, 973–993 (2015).

51. Schmittner, A. & Somes, C. J. Complementary constraints from carbon (13C) and nitrogen (15N) isotopes on the glacial ocean's soft-tissue biological pump. *Paleoceanography* **31**, 669–693 (2016).

52. Muglia, J., Somes, C. J., Nickelsen, L. & Schmittner, A. Combined effects of atmospheric and seafloor iron fluxes to the glacial ocean. *Paleoceanography* **32**, 1204–1218 (2017).

53. Schmittner, A. & Egbert, G. D. An improved parameterization of tidal mixing for ocean models. *Geosci. Model Dev.* **7**, 211–224 (2014).

54. Peltier, W. Global glacial isostacy and the surface if the ice-age earth: The ICE-5G (VM2) model and Grace. *Annu. Rev. Earth Planet. Sci.* **32**, 111–149 (2004).

55. Argus, D. F., Peltier, W. R., Drummond, R., Moore, A. W. & Argus, D. F. The Antarctica component of postglacial rebound model ICE-6G_C (VM5a) based on GPS positioning, exposure age dating of ice thicknesses, and relative sea level histories. *Geophys. J. Int.* **198**, 537–563 (2014).

56. Peltier, W. R., Argus, D. F. & Drummond, R. Space geodesy constrains ice age terminal deglaciation: the global ICE-6G_C (VM5a) model. *J. Geophysi. Res. Solid Earth* **120**, 450–487 (2015).

57. Saenko, O. A. & Weaver, A. J. What drives heat transport in the Atlantic: sensitivity to mechanical energy supply and buoyancy forcing in the Southern Ocean. *Geophys. Res. Lett.* **31**, L20305 (2004).

58. Danabasoglu, G. et al. North Atlantic simulations in coordinated ocean-ice reference experiments phase II (CORE-II). Part I: mean states. *Ocean Model.* **73**, 76–107 (2014).

59. Key, R. M. et al. A global ocean carbon climatology: results from global data analysis project (GLODAP). *Global Biogeochem. Cycles* **18**, 1–23 (2004).

60. Wilmes, S.-B., Green, J. A. M. & Schmittner, A. Data from 'Enhanced vertical mixing in the glacial ocean inferred from sedimentary carbon isotopes'. *Zenodo* https://doi.org/10.5281/zenodo.4704627 (2021).

61. Wilmes, S.-B., Green, J. A. M. & Schmittner, A. Glacial ice sheet extent effects on tidal mixing and the global overturning circulation - Model Output. *Zenodo* https://doi.org/10.5281/zenodo.1139242 (2019).

Author contributions
SBW and AS conceived and planned the simulations. SBW carried out the simulations and analyzed them with help from AS and JAMG. SBW took the lead writing the paper and all authors discussed the results and contributed to the final paper.

Competing interests
The authors declare no competing interests.

Additional information
Supplementary information The online version contains supplementary material available at https://doi.org/10.1038/s43247-021-00239-y.

Correspondence and requests for materials should be addressed to S.-B.W.

Peer review information *Communications Earth & Environment* thanks the anonymous reviewers for their contribution to the peer review of this work. Primary Handling Editor: Heike Langenberg. Peer reviewer reports are available.

Reprints and permission information is available at http://www.nature.com/reprints

Publisher's note Springer Nature remains neutral with regard to jurisdictional claims in published maps and institutional affiliations.